Cesium vacancy ordering in phase-separated $Cs_xFe_{2-y}Se_2$

K. M. Taddei,[1,2,*] M. Sturza,[2,†] D. Y. Chung,[2] H. B. Cao,[3] H. Claus,[2] M. G. Kanatzidis,[2,4] R. Osborn,[2] S. Rosenkranz,[2] and O. Chmaissem[1,2]

[1]*Physics Department, Northern Illinois University, DeKalb, Illinois 60115, USA*

[2]*Materials Science Division, Argonne National Laboratory, Argonne, Illinois 60439, USA*

[3]*Quantum Condensed Matter Division, Oak Ridge National Laboratory, Oak Ridge, Tennessee 37831, USA*

[4]*Department of Chemistry, Northwestern University, Evanston, Illinois 60208-3113, USA*

(Received 21 July 2015; published 14 September 2015)

By simultaneously displaying magnetism and superconductivity in a single phase, the iron-based superconductors provide a model system for the study of magnetism's role in superconductivity. The class of intercalated iron selenide superconductors is unique among these in having the additional property of phase separation and coexistence of two distinct phases—one majority phase with iron vacancy ordering and strong antiferromagnetism, and the other a poorly understood minority microscopic phase with a contested structure. Adding to the intrigue, the majority phase has never been found to show superconductivity on its own while the minority phase has never been successfully synthesized separate from the majority phase. In order to better understand this minority phase, a series of high-quality $Cs_xFe_{2-y}Se_2$ single crystals with $(0.8 \leqslant x \leqslant 1; 0 \leqslant y \leqslant 0.3)$ were grown and studied. Neutron and x-ray powder diffraction performed on ground crystals show that the average $I4/mmm$ structure of the minority phase is distinctly different from the high-temperature $I4/mmm$ parent structure. Moreover, single-crystal diffraction reveals the presence of discrete superlattice reflections that remove the degeneracy of the Cs sites in both the majority and minority phases and reduce their structural symmetries from body centered to primitive. Group theoretical analysis in conjunction with structural modeling shows that the observed superlattice reflections originate from three-dimensional Cs vacancy ordering. This model predicts a 25% vacancy of the Cs site in the minority phase which is consistent with the site's refined occupancy. Magnetization measurements performed in tandem with neutron single-crystal diffraction provide evidence that the minority phase is the host of superconductivity. Our results also reveal a superconducting dome in which the superconducting transition temperature varies as a function of the nominal valence of iron.

DOI: 10.1103/PhysRevB.92.094505 PACS number(s): 61.05.cf, 61.05.fg, 74.70.Xa, 75.50.Ee

I. INTRODUCTION

In recent years, the microscopic coexistence of superconductivity and magnetism in iron-based superconductors has attracted intense interest from the condensed matter physics community [1–4]. In particular, the 122 member (e.g., $BaFe_2As_2$) of the iron pnictide family, with the common "$ThCr_2Si_2$" structure and composition of (A,A') $(Fe,B)_2As_2$ (where A,A', and B represent alkali metals, alkaline-earth metals, and transition metals, respectively) has provided fertile ground for the exploration of superconductivity due to the relative ease with which its members can be synthesized and its stability under numerous doping regimes. Consequently, it is now well established that a narrow region of phase space exists in the electron- and hole-doped members of these materials in which superconductivity and magnetism strongly compete just before the system crosses into a purely superconducting state upon further doping [5–9]. An in-plane magnetic spin-density wave (SDW) phase produced by Fermi surface nesting is found to lose strength upon doping, with the Néel transition temperature T_N getting progressively suppressed into a superconducting state which persists and reaches a maximum T_c with further doping [10–12]. In recent work, we demonstrated that the competition between magnetism and superconductivity is even more surprising and complex than previously thought with the discovery of a tetragonal magnetic ground state known as the C_4 phase in yet another narrow compositional region within the established phase coexistence pocket [13]. This discovery further develops the narrative of competition between magnetism and superconductivity showing the rich behavior in these systems and the close coupling between magnetism and structure. Therefore, determining the structural details of superconducting phases that arise from a magnetic phase is of great importance towards achieving a better understanding of the exact mechanism of superconductivity, in general, and more specifically of the iron-based superconductors.

While the work done on the iron pnictides has led to the development of a universal phase diagram with relatively well-understood properties, the related family of intercalated iron selenides has proven more opaque. Though isostructural to the pnictide family at high temperatures, the iron selenides show striking differences: They have a Fermi surface morphology devoid of the Γ hole pocket thought to be vital to the superconducting pairing in the pnictides, a strong AFM ordering with T_N more than twice that of the iron pnictides, and a large magnetic moment that would appear to indicate a Mott insulator; in addition they also exhibit two distinct coexisting phases, with radically different properties [14–17].

Phase separation in the intercalated iron selenides is well established and this induction of microscopic domains of

*Corresponding author: ktaddei@anl.gov

†Present address: Leibniz Institute for Solid State and Materials Research Dresden IFW, Institute for Solid State Research, 01069 Dresden, Germany.

minority 122-type structure in a host matrix with robust magnetic properties is unique and interesting [17–22]. Though its formation is widely reported, the exact nature of this minority phase remains debated, being described as isostructural with the higher-temperature paramagnetic 122 phase from x-ray diffraction on polycrystalline $K_xFe_{2-y}Se_2$ or as being distorted to lower orthorhombic or monoclinic symmetries as found in x-ray diffraction on $Rb_xFe_{2-y}Se_2$ and $Cs_xFe_{2-y}Se_2$ single crystals, respectively [18,19,23]. Other studies of $K_xFe_{2-y}Se_2$ have reported the formation of a new "234" phase, which may be unique to the K-intercalated family or perhaps simply related to the growth conditions of that particular crystal [24].

At temperatures above ~500 K the intercalated $A_xFe_{2-y}Se_2$ family of iron selenide superconductors (where A = K, Cs, or Rb) orders into the typical "122" $ThCr_2Si_2$ structure with the $I4/mmm$ space group symmetry in which the Fe and A site vacancies are fully disordered [25]. Upon cooling, the iron vacancies begin to order, driving first a structural transition at T_s into a larger $\sqrt{5} \times \sqrt{5} \times 1$ supercell with a lower $I4/m$ space group symmetry and second, a magnetic transition into an antiferromagnetic (AFM) block-checkerboard phase at a slightly lower temperature [25]. The formation of the vacancy-ordered supercell produces a majority phase with the $A_2Fe_4Se_5(A_{0.8}Fe_{1.6}Se_2)$ stoichiometry (245 phase). Concurrently, the excess cations segregate into a minority phase identified as $A_xFe_2Se_2$ of the 122 structural type. Hereafter, we will use the term LT122 to distinguish the minority phase from the high-temperature paramagnetic 122 phase or HT122.

In this paper, we will describe the synthesis of high-quality $Cs_xFe_{2-y}Se_2$ single crystals and demonstrate the ordering of Cs vacancies in both the antiferromagnetic majority 245 and the superconducting minority LT122 phases. Superstructure formation due to long-range ordering of the Cs vacancies is observed as sharp superlattice reflections in contrast to the commonly seen out-of-plane intensity rods [18,20,21,26]. Modeling based on group theoretical representation analysis shows that three-dimensional Cs vacancy ordering takes place in the ab plane and at alternating layers along the c axis in both the majority and minority phases.

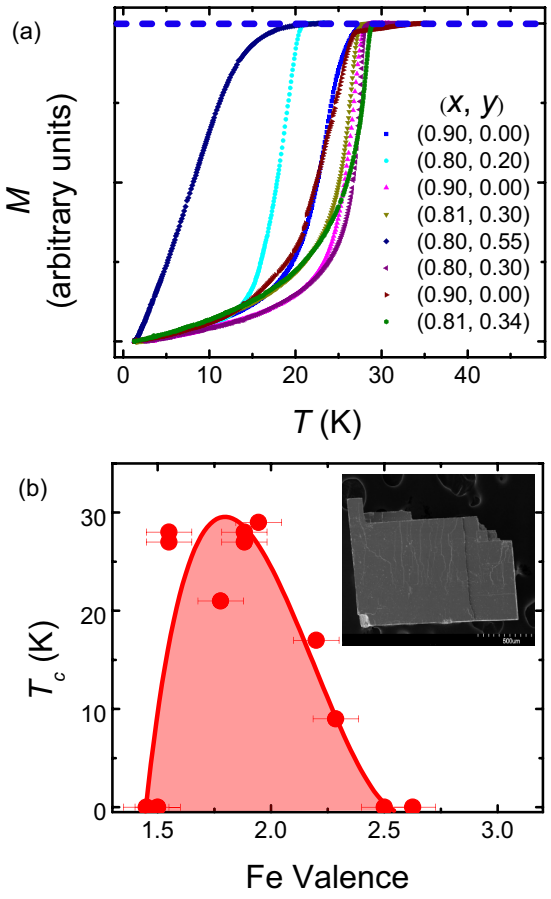

FIG. 1. (Color online) (a) Magnetization measurement data for a series of $Cs_xFe_{2-y}Se_2$ single crystals showing sharp single-step superconducting transitions, normalized for visual clarity irrespective of superconducting volume fraction, with transition onsets (T_c) between 9 and 30 K. (b) The variation of T_c onset plotted as a function of Fe valence shows the presence of a superconducting dome of approximately inverse parabolic shape. Inset shows image of a representative single crystal (Fe valence values were calculated from the nominal compositions).

II. METHODS

Single crystals of cesium-intercalated iron selenides with nominal compositions $Cs_xFe_{2-y}Se_2(0.8 \leqslant x \leqslant 1; 0 \leqslant y \leqslant 0.3)$ were prepared from metallic Cs and Fe powder, and crushed Se shots (Aldrich, 99.95%, 99.999%, and 99.99%, respectively). Due to the materials' sensitivity to air and moisture, all work, chemical handling, and storage were performed in a dry argon-filled glove box. All reactions were carried out in quartz or niobium tubes sealed under vacuum or flowing argon gas, respectively. FeSe precursors were prepared by intimately mixing and annealing the desired stoichiometric ratios of Fe and Se powders at 700 °C for 2 h in sealed carbon-coated quartz tubes. The resultant reground $Fe_{2-y}Se_2$ product was loaded together with appropriate amounts of the Cs metal into two opposite ends of an H-shaped quartz tube. Both ends were sealed with the Cs side kept at liquid nitrogen temperatures to prevent evaporation while sealing. The tube was subsequently annealed at 250 °C for 24 h, then ramped to 400 °C where it was kept at this temperature for 48 h. At the end of the heat treatment, all of the Cs metal had completely transferred to the $Fe_{2-y}Se_2$ side to produce an inhomogeneous mixture. After grinding, the mixture was loaded and sealed inside an alumina crucible placed within a niobium tube which, in turn, was loaded and sealed in an evacuated quartz tube and fired at 1120 °C for 12 h, followed by slow cooling to 650 °C at a rate of 5 °C/h and then rapid cooling to room temperature. Black crystal rods were obtained that could be easily cleaved into platelets with flat shiny surfaces [see Fig. 1(b) inset]. The crystal's c axis is perpendicular to the surface of these platelets. Microprobe analyses of the $Cs_xFe_{2-y}Se_2$ crystals were performed using a Hitachi S-4700-II scanning electron microscope (SEM) in the backscattered and secondary electrons modes. Powder samples were obtained by carefully grinding a suitable mass of the high-quality single crystals.

Temperature-dependent four-probe resistivity measurements were performed at temperatures between 1.8 and 300 K using a Quantum Design Physical Properties Measurement

System (PPMS). Electrical contacts were mounted on the single crystals in an Ar-filled glove box. A home-built low-field superconducting quantum interference device (SQUID) magnetometer was used to measure the dc magnetization [27]. A few well-shaped crystals were selected for single-crystal x-ray and neutron diffraction experiments.

Single-crystal x-ray diffraction data were collected at room temperature using a STOE imaging plate diffraction system (IPDS-II) and the monochromatic Mo-$K\alpha$ radiation ($\lambda = 0.710\,73$ Å). Individual frames were collected with a 4-min exposure time and 1° ω rotations.

Single-crystal neutron diffraction was performed on the four-circle neutron diffractometer, HB-3A, at the High Flux Isotope Reactor (HFIR) of Oak Ridge National Laboratory (ORNL). The neutron wavelength of 1.542 Å was used from a bent perfect Si-220 monochromator [28]. A total of 470 reflections were collected including the $\sqrt{5} \times \sqrt{5}$ superlattice peaks and used in the FULLPROF software suite for model refinement [29]. The measured crystal was mounted in a glove box and coated with a thin layer of CYTOP to prevent oxidation. Time-of-flight neutron powder diffraction was performed on the POWGEN beamline of the Spallation Neutron Source at ORNL. Data were collected on warming first in coarse steps at 10, 150, and 300 K and then in relatively finer steps up to 550 K. High-resolution synchrotron powder diffraction data ($\lambda = 0.413$ Å) were also collected at Argonne National Laboratory using the beamline 11-BM-B of the Advanced Photon Source (APS). Rietveld structural refinements were performed using the General Structural Analysis System (GSAS) and EXPGUI [30,31].

III. RESULTS AND DISCUSSIONS

A. Superconductivity and phase separation

Magnetization measurements displayed in Fig. 1(a) show typical single-step superconducting transitions for a series of crystals $Cs_xFe_{2-y}Se_2$ ($0.8 \leqslant x \leqslant 0.9$, $0 \leqslant y \leqslant 0.55$). Careful control of the nominal composition allowed for the controlled growth of high-quality crystals with either superconducting or nonsuperconducting properties. Interestingly, unlike the K and Rb iron selenides which exhibit a superconducting "plateau" in their respective phase diagrams, our Cs-based samples with differing iron valence show different T_c's creating a superconducting dome for iron valence v: $1.55 \leqslant v \leqslant 2.29$ [Fig. 1(b)] [32,33]. Many crystals with superconducting T_c's ranging between 9 and 30 K were examined using single-crystal diffraction. Select crystals were ground into fine powders for neutron and x-ray powder diffraction measurements. Interestingly, the ground superconducting crystals lose their superconductivity (measurements of the nonsuperconducting powders not shown here). We will relate in subsequent paragraphs the superconducting properties of the crystals to the integrity and microstructure of the minority LT122 phase.

Figures 2(c)–2(f) show high-resolution room temperature neutron and x-ray powder diffraction patterns (of nominal composition $Cs_{0.9}Fe_2Se_2$) with the main peaks of the "245" phase indexed. Arrows indicate reflections that the majority phase fails to index, as they belong to the minority LT122 structure in agreement with earlier reports on similar materials

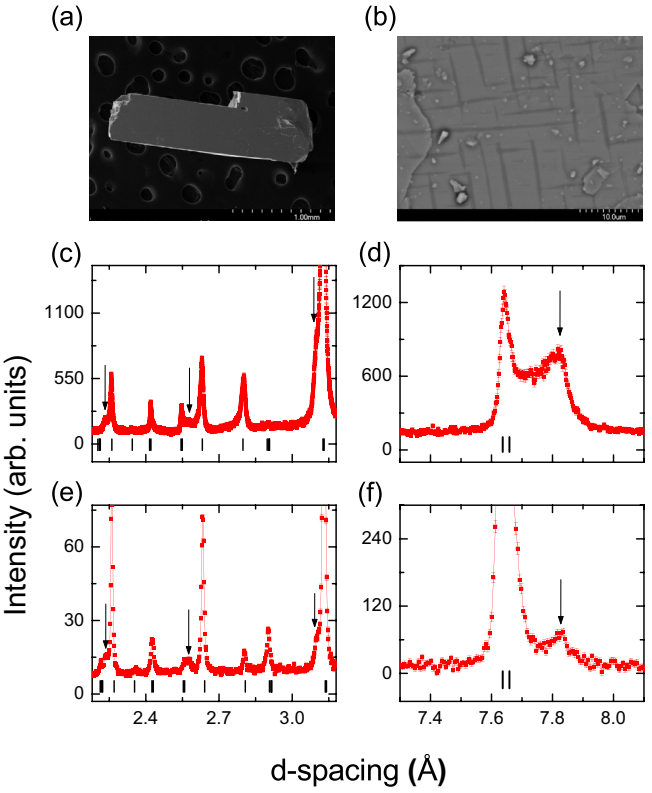

FIG. 2. (Color online) SEM images of a $Cs_{0.9}Fe_2Se_2$ single crystal (a) showing the presence of the LT122 phase as microscopic needles embedded in a host matrix of the 245 phase (b) (images are taken of the crystallographic ab plane). Powder patterns from high-resolution synchrotron x-ray (c, d) and neutron (e, f) diffraction. Peaks of the 245 phase are indexed. A series of unindexed peaks, indicated by arrows, belonging to the LT122 phase are seen near the 245 peaks indicating a related structure with slightly different lattice parameters.

of phase separation and coexistence. No trace of other byproducts is observed including the 234 phase proposed by Li *et al.* [24].

To determine the exact makeup and structure of the minority LT122 phase, Rietveld refinements were performed examining all the previously reported structural models [18,19,23]. An LT122 weight fraction in the range of 5%−30% was determined from the refinements in all of our examined samples. Refinements of the LT122 structure using the tetragonal $I4/mmm$ symmetry resulted in the lowest R_{wp} and χ^2 values with no visual or statistical improvements to the fit obtained upon the introduction of the proposed orthorhombic or monoclinic distortions within the limits of signal to background and Q resolution of our data. However, as will be described later, this phase is distinctly different from the high-temperature paramagnetic $I4/mmm$ HT122 structure. Figures 2(d) and 2(f) show the relatively broad and asymmetric peaks of the LT122 minority phase, a feature that is consistent throughout the measured temperature range which may be attributed to microscopic domain sizes, strains, stacking faults, and other similar factors commonly seen in the selenides. Scanning electron microscope (SEM) backscattering measurements show the LT122 phase morphology as small needlelike domains

oriented in the a or b directions of the crystal with approximate dimensions of $\sim 10 \times 0.1 \mu$m embedded in a host matrix of the majority phase [see Figs. 2(a) and 2(b), for example]. When ground into powders, such microscopic fragments explain well the observed broadening of the LT122 phase peaks as described by the Scherrer equation [34]. Peak broadening could also be related to some expected chemical inhomogeneity among the isolated LT122 domains that result from the phase separation. Similar conclusions have been supported by energy-dispersive x-ray (EDX) measurements for several $Cs_xFe_{2-y}Se_2$ crystals but interestingly not in the $K_xFe_{2-y}Se_2$ counterparts [35,36].

B. Structural details

Select room temperature structural parameters obtained from neutron single-crystal diffraction (HB3A), neutron powder diffraction (POWGEN), and synchrotron x-ray powder diffraction (11BMB) are displayed in Table I. As the table shows, consistent results are obtained from the different techniques, especially regarding the nature of phase separation and site occupancies. Of particular interest is the ordering of the Fe vacancies and the fact that the "vacant" Fe site is not completely empty. We will later discuss the additional ordering of the refined Cs vacancies.

Figure 3(a) shows the temperature dependence of the nuclear 002 peak (indexed in the high-temperature $I4/mmm$ structure). On cooling, the peak shifts at 530 K to higher d spacing indicating a first-order-like discontinuous negative thermal expansion of the c axis. This behavior is better seen in the refined lattice parameters plots in Figs. 4(a) and 4(b) or the instrument-independent c/a ratio [Fig. 4(d)] which also provides a measure of the lattice anisotropy. As the figure demonstrates, the c/a ratio increases suddenly at the transition temperature 530 K consistent with the abrupt changes in the majority phase's lattice parameters and in agreement with the expected ordering of the Fe vacancies and the consequential resizing of the unit cell. The anisotropy of the a and c lattice parameters has a compensating effect leaving the unit cell volume nearly continuous [Fig. 4(c)], but with a slight change in slope at the transition temperature. The migration and ordering of vacancies from the richer Fe stoichiometry of the HT122 single phase causes the $FeSe_4$ tetrahedra in the majority 245 phase to contract and expand in the in-plane and the out-of-plane directions, respectively [Fig. 5(a)], and leads to displacing the selenium ions about 0.1 Å farther away from the Fe planes as shown in Fig. 5(c).

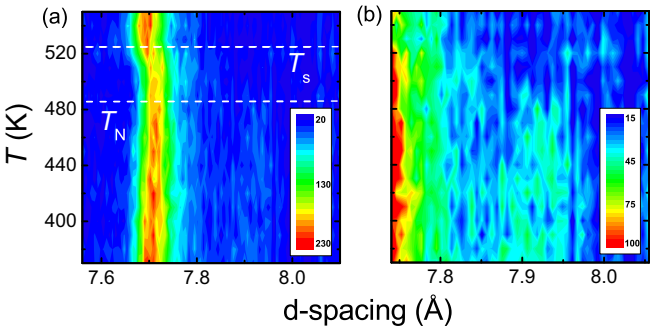

FIG. 3. (Color online) Diffractogram following the temperature dependence of the (002) structural peak (indexed using the HT122 $I4/mmm$ tetragonal structure) with the structural and magnetic transitions indicated. Panel (b) shows a rescaled plot of d spacing just beyond the 245 phase's (002) peak showing the entrance of the LT122 phase's (002) peak.

The LT122 phase becomes visible in the neutron powder diffraction data only below 490 K shortly after the structural transition has occurred [Fig. 3(b)], though its initial inception should coincide with the primary structural transition at 530 K. The small 5%−6% weight fraction of the minority LT122 phase and the submicroscopic-sized domains, especially during formation, coupled with low signal-to-noise ratio from the high-temperature furnace runs may all contribute to delaying the unambiguous detection of this phase in the diffraction patterns between 490 and 530 K. As shown in Figs. 4(a)–4(d), the a and c lattice parameters of the LT122 phase undergo significant −3% contraction and +3% expansion, respectively. The markedly different lattice parameters indicate that the LT122 is a unique distinct phase which is not a continuation of the HT122 Cs and Fe disordered phase. Published reports on comparable single crystals have shown that a similar low-temperature 122 phase grows in diverse morphologies and sizes with its c axis along the (110) direction of the 245 matrix [36]. However, our single-crystal screening diffraction measurements performed on many crystals have always shown the two c axes to be coaligned; see Fig. 6, for example. Similar to the 245 phase, the lattice parameters' properties of the LT122 phase can be explained as a consequence of the migrating iron vacancies leaving behind Fe-rich clusters

TABLE I. Lattice parameters, phase fractions, and occupancies of LT122 and 245 phases from model refinements performed on x-ray powder, neutron powder, and neutron single-crystal diffraction data. Summed phase fractions of less than 100% are due to the presence of impurity phases.

		245 phase $I4/m$							LT122 phase $I4/mmm$			
Sample	wRp	Lattice (Å)	Cs ($2a$)	Cs ($8h$)	Fe ($16i$)	Fe ($4d$)	$Mz(\mu_B$/Fe)	Phase fraction	Lattice (Å)	Cs ($2a$)	Fe ($4d$)	Phase fraction
$Cs_{0.8}Fe_{1.7}Se_2$	7.09%	$a = 8.8494(1)$	0.742 (6)	0.787(2)	0.933(3)	0.064(9)	–	72.22 (7)%	$a = 3.8503(1)$	0.745 (4)	0.999 (3)	27.78(9)%
11BM (300 K)		$c = 15.2987(3)$							$c = 15.6468(5)$			
$Cs_{0.9}Fe_2Se_2$	5.30%	$a = 8.85734(7)$	0.95(3)	0.89(8)	0.983(2)	0.157(8)	2.53(3)	93.3(5)%	$a = 3.8501(3)$	0.73(7)	0.96(3)	6.6(3)%
POWGEN (300 K)		$c = 15.2495(2)$							$c = 15.2495(2)$			
$Cs_{0.8}Fe_{1.7}Se_2$	15%	$a = 8.83$[a]	0.944(1)	0.744(5)	1[a]	0.04(1)	3.372(7)	–	–	–	–	–
HB3A (30 K)		$c = 15.199$[a]										

[a]Values not refined.

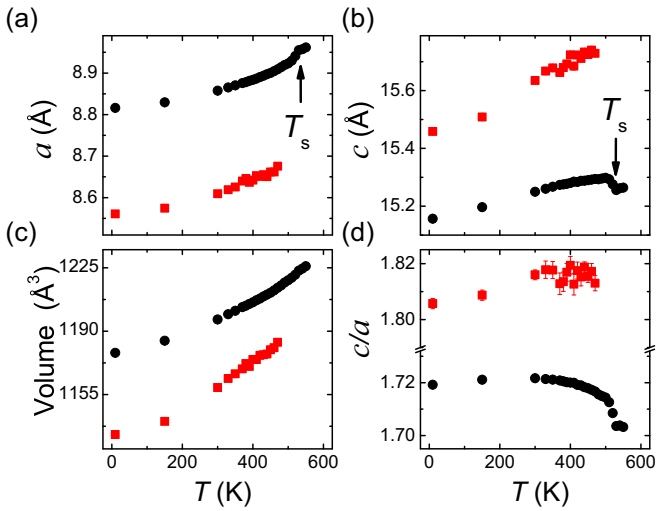

FIG. 4. (Color online) T dependence of the (a) a lattice parameter, (b) c lattice parameter, and (c) volume of the main HT122 and 245 phases as well as the LT122 phase (in black and red, respectively). Linear fits have been plotted to demonstrate the lattice parameters' discontinuity at the structural transition (T_s). (d) T dependence of the lattice anisotropy measured in the c/a ratio. In all plots and calculated values, the a lattice parameter of the high- and low-temperature 122 phases has been scaled by $\sqrt{5}$ to aid in visual comparison to the 245 phase.

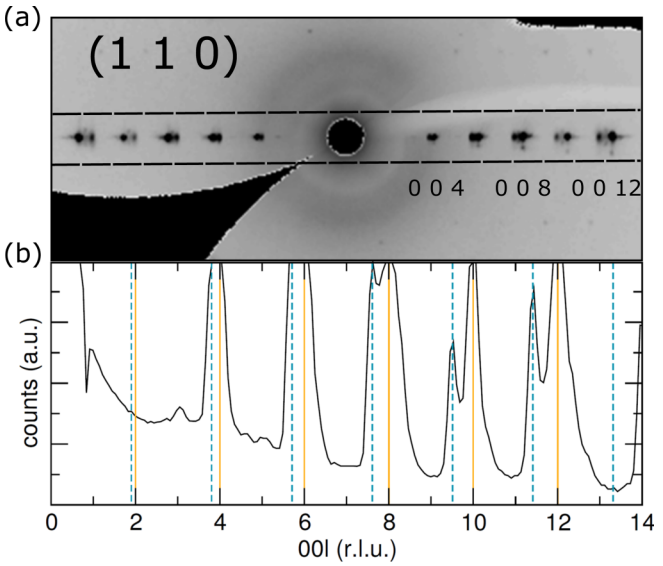

FIG. 6. (Color online) Panel (a) shows the doubling of the (00l) reflections at 300 K indicating the LT122 and 245 phases' relative alignment. Panel (b) shows an integrated line cut through these reflections with the LT122 phase and 245 phase peaks denoted by dotted blue and solid yellow lines, respectively. The LT122 peaks can be seen diverging at higher relative lattice units (r.l.u.) due to its slightly larger c lattice parameter.

that separate to form the minority 122-type phases in which the iron site is expected to be fully occupied while the Cs site would exhibit significantly more vacancies than in the high-temperature 122 phase. Indeed, our refinements show

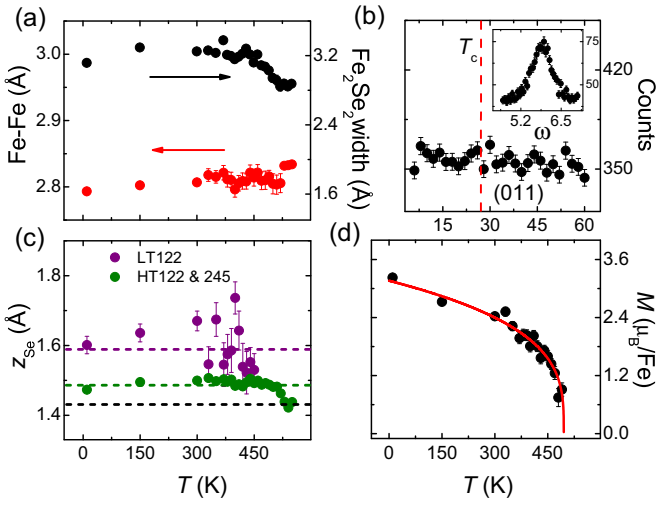

FIG. 5. (Color online) (a) T dependence of average iron-to-iron bond length (red symbols—left axis) and of the average selenium-to-selenium distance within a single Fe_2Se_2 layer (black symbols—right axis). (b) Temperature dependence of magnetic (011) peak shown across the superconducting transition (28 K); inset shows an ω scan through the (001) peak, number of counts has been scaled by $\frac{1}{10}$. (c) T dependence of the average selenium position for all phases with black, green, and purple dotted lines as guides to the eye for the HT122, 245, and LT122 phases, respectively. (d) T dependence of the iron magnetic moment fit by the power law $M(T) = A\frac{(T_N-T)^\beta}{T_N}$.

that the Fe site is fully occupied within one standard deviation while the Cs occupancy rate is only ~75% of the total available sites (see Table I). We note that this trend is in agreement with several reported studies, but the exact amount of Cs vacancies change wildly from one sample to another [26,37,38]. The proper fractional amount of Cs vacancies (25% of the available sites) in our sample is quite interesting because one may expect some cationic ordering to occur. While we do not see extra reflections in the powder diffraction patterns that corroborate such ordering, they are clearly present in the single-crystal x-ray diffraction data, as described in Sec. III D. The significant departure of the a and c lattice parameters of the LT122 phase is thus further understood as due to substantially different chemical composition and cationic ordering (when compared to HT122) which are likely to result in adjusted internal bond lengths and the corresponding unit cell. Figure 5(c), for example, shows that the Se ions are ~0.2 Å above or below the Fe planes. Strains associated with the LT122 needles being sandwiched between large parts of the host 245 matrix [see Fig. 2(b)] could also contribute to the large elongation of the c axis (perpendicular to the needles) and the concomitant contraction of the a and b axes. The LT122 unit cell volume behavior shown in Fig. 4(c) has a coefficient of thermal expansion $\alpha = \frac{1}{V_0}(\frac{V_0-V}{T_0-T}) = 1.24 \times 10^{-4}$ K^{-1} higher than that of the 245 phase (1.16×10^{-4} K^{-1} in the 470–520 K temperature range) or the HT122 phase (1.01×10^{-4} K^{-1} between 530 and 550 K).

C. Magnetism

$Cs_xFe_{2-y}Se_2$ exhibits the lowest Néel temperature (490 K) among the known isoelectronic $A_xFe_{2-y}Se_2$ superconducting

iron selenides (i.e., A = Na, K, Rb, or Cs). This series exhibits a clear relationship between T_N and the A-site ionic radius (r_A), with T_N (595, 560, 500, and 490 K) decreasing with increasing r_A (for Na, K, Rb, and Cs) [25,39,40]. The increased ionic radius is also reflected in the significant expansion of the c axis (~13.25, 14.0, 14.6 Å, and 15.3 Å, for Na, K, Rb and Cs, respectively) [21,25,41]. The large Cs cations push the FeSe layers farther apart than do their K, Rb, or Na analogs, thus lessening the strength of interlayer antiferromagnetic interactions and partially suppressing the associated antiferromagnetic transition temperatures.

Satisfactory fits and agreement factors were obtained using POWGEN and HB3A data to model the well-known block-antiferromagnetic checkerboard structure using the corresponding magnetic space group $I4/m'$ [25,42]. At 10 K, the magnetic moment of the occupied iron site of the 245 phase refined to 3.23(6)μ_B/Fe (POWGEN) and 3.37(7) μ_B/Fe (HB3A), Table I, in excellent agreement with the reported magnetic moment in pure $Cs_2Fe_4Se_5$ (3.4 μ_B/Fe) [40]. By fitting the temperature dependence of the refined magnetic moment to the power law $M(T) \propto (T_N - T)^{\beta}/T_N$ the critical exponent and Néel temperature were determined to be 0.30(2) and 490(6) K, respectively. The large value of the critical exponent β indicates strong three-dimensional magnetic correlations despite the larger Cs ionic size and the elongated c axis, and in clear contrast with the analogous arsenic-based superconductors for which lower β values have been consistently obtained indicative of strong magnetoelastic coupling [7,43]. It is worth noting here that in contrast to the iron pnictides, the magnetic and nuclear structural transitions are completely decoupled in the iron selenides.

On the other hand, it is well established in the phase diagrams of both the hole-doped and electron-doped iron arsenides that magnetism is partially or fully suppressed when entering the superconducting dome due to the two states competing for the same electrons [5]. By analogy, we expect to see a decrease in the intensity of magnetic reflections below T_c should the 245 phase be superconducting. Figure 5(b) shows the integrated intensity of the magnetic 011 reflection that belongs to the 245 phase; the constant flat data within the experimental error bars clearly demonstrate the magnetic 245 phase as being uncorrelated with the measured superconductivity in the crystal. Likewise, monitoring the integrated intensities of the nuclear 620 reflection yielded a featureless behavior (data not shown). We therefore conclude that superconductivity in our crystals correlate with the LT122 phase in agreement with the observation made above of ground crystals losing their superconductivity.

While the magnetic structure of the majority 245 phase is well understood, controversy remains regarding the magnetic character of the minority phase. The small 5% fraction of the minority phase in our single-crystal sample makes direct diffraction measurements of its magnetic properties very difficult, but recent computational work by Luo and co-workers suggested that the 122 structure in the intercalated iron selenides should be magnetic and that strong correlations between the selenium position and the magnetic ground state should exist [44]. The position of the selenium atoms may then become a useful indicator of the magnetic character of the minority phase. Figure 5(c) shows the z position of the selenium atoms extracted from the Rietveld refinements. The use of a polynomial fit to the z_{Se} of the LT122 phase allows us to extrapolate the position down to zero Kelvin: $z_{Se}(T = 0) = 1.58(4)$ Å. While this agrees with Luo and co-workers' predicted selenium position for a ferromagnetic LT122 configuration, $z_{Se} = 1.586$ Å, it is clearly different from $z_{Se} = 1.517$ Å, the value calculated for the lowest-energy configuration of the antiferromagnetic spin-density wave stripe structure [44]. In theory, the existence of Cs vacancies in the LT122 phase, described below, together with the anisotropic contraction of the c lattice parameter could drive the system into an electronic structure consistent with higher-energy ferromagnetic ground state; however, we have never observed any ferromagnetic signal in our magnetization measurements. This disagreement between Luo's model which relates to materials with full 122 stoichiometry and our measurements may be due to the Cs vacancies and their effect on both the structure and electronic configuration of these materials. We note that the ordering of Fe vacancies in the 245 phase produces similar effects, to a lesser extent, with the z_{Se} being pushed to higher values than in the HT122 phase [Fig. 5(c)].

Neutron diffraction measurements have been used to suggest the tunable ground state of the LT122 phase [45]. Zhao *et al.* monitored two superlattice peaks (103 and 105) that belong to the semiconducting LT122 phase in their nonsuperconducting $K_xFe_{2-y}Se_2$ crystal and found that the peaks' integrated intensities display a clear anomaly at ~280 K which they define as the onset transition temperature to an in-plane SDW antiferromagnetic ground state associated with LT122, similar to that of $BaFe_2As_2$, for example. The authors noted that the extra peaks did not disappear until ~450 K and suggested a rhombus iron vacancy-ordered 122 structure to explain their persistent presence and nuclear origin. The authors also noted that the integrated intensities of similar peaks visible in their superconducting sample did not exhibit any anomaly at 280 K and that they remain roughly unchanged up to 450 K which they attributed to a suppression of the rhombus iron vacancy-ordered model in the superconducting samples. In the next section we will show that similar peaks were observed in our $Cs_xFe_{2-y}Se_2$ samples together with other superlattice reflection sets. While we recognize the chemical and synthesis differences between our Cs-based samples and the K-based crystals in Ref. [45] our results find that Cs ordering accounts for all the extra reflections. Obviously, the complex nature of this system could make the LT122 magnetic ground state strongly dependent on the growth conditions and the resulting intercalating ionic concentrations and stoichiometry. Further studies are needed targeting the isolation and synthesis of pure LT122 with varying stoichiometries (i.e., fully occupied Fe sites and significant Cs vacancies) and physical properties.

D. Cesium vacancy ordering and superstructure formation

Neutron and x-ray single-crystal diffraction data from all the examined crystals show the well-known 245 superstructure peaks as in the powder diffraction patterns. However, reciprocal space cuts reconstructed from the x-ray single-crystal diffraction data reveal the presence of faint reflections (up to ~2% of the maximum observed intensity) that violate both the body-centered $I4/mmm$ and $I4/m$ space group symmetries of

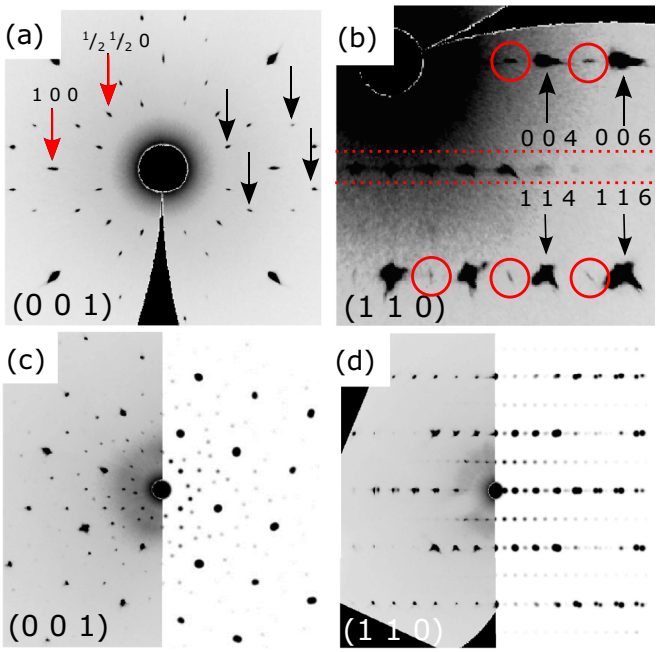

FIG. 7. (Color online) Cuts through reciprocal space showing the presence of (a) superlattice reflections indicative of Fe vacancy ordering in the 245 structure (black arrows) as well as extra reflections at $(\frac{1}{2}\ \frac{1}{2}\ 0)$ and (010) forbidden by the $I4/m$ symmetry (red arrows) in a [0 0 1] cut. Seen in the [1 1 0] plane are further forbidden reflections at (hhl; with l odd) indicated by red circles (b). In this orientation the $(\frac{1}{2}\frac{1}{2}l)$ reflections (visible between the dotted red lines) can be seen to have fractional l components incommensurate with the (00l) reflections of the 245 phase. Panels (c, d) show comparisons of the observed and modeled patterns in the two orientations; all peaks are found to be reproduced by two 245 twin domains as well as the proposed LT122 superstructure (see text for more details). All panels are of the same crystal; superlattice reflections which are not visible in (d) but can be seen in (b) are not clearly seen in the former's intensity scale.

the minority and majority phases, respectively. The intensities of these reflections are too weak to detect with clarity in the powder diffraction patterns so average $I4/mmm$ and $I4/m$ structures may still satisfactorily be used in the refinements.

The full indexing of the crystal diffraction data has been somewhat complicated by the presence of twins and the fact that the related lattice parameters of the 245 and LT122 phases result in many nearly degenerate reflections. While the overlapping in-plane main reflections of the two phases are harder to resolve, the difference in their c axes is large enough to separate the (00l) reflections, especially at large diffraction angles [Figs. 6(a) and 6(b)], and to estimate the respective lattice parameters for each phase.

Additionally, we note the presence of extra in-plane $(\frac{1}{2}\ \frac{1}{2}\ 0)$ and (0 1 0) type reflections and out-of-plane $(\frac{1}{2}\ \frac{1}{2}\ l)$, $(\frac{3}{2}\ \frac{3}{2}\ l)$ together with very faint (hhl; with $h = 0,1$ and $l =$ odd integers) reflections all indexed using the tetragonal $a \times a \times c$ unit cell of the parent 122 structure; see Fig. 7, for example. The sharp out-of-plane reflections, albeit very weak, indicate the existence of significant interlayer correlations.

To the best of our knowledge, the often referred to $\sqrt{2}a \times \sqrt{2}a \times c$ LT122 superstructure has not been described in detail beyond being another version of the stoichiometric 122 phase but clearly with random Cs or Fe vacancies. In a recent publication, [26] possible two-dimensional ordering of Cs has been suggested in a similar $Cs_{0.8}Fe_{1.6}Se_2$ crystal showing the typical LT122 superstructure reflections in the [001] plane but displaying the common intensity rods in the out-of-plane reciprocal space cuts [18,20,21,26]. The authors performed *ab initio* calculations that suggest possible Cs ordering that must be randomized at different planes to produce the intensity rods. Possible ordering of the A site in this LT122 structure has also been alluded to in other related compositions but without further details [18]. In this work, a $P4/mmm$ superstructure of the same $\sqrt{2}a \times \sqrt{2}a \times c$ unit cell size has been constructed and used for detailed crystal diffraction simulations. The primitive lattice is necessary to produce the body-centered forbidden superlattice reflections. In this space group, cesium atoms occupying the Wyckoff $2a$ sites in the parent $I4/mmm$ space group split into three independent Wyckoff sites with Cs1 at $1a$ (000), Cs2 at $1c$ $(\frac{1}{2}\ \frac{1}{2}\ 0)$, and Cs3 at $2e$ $(0\ \frac{1}{2}\ \frac{1}{2})$.

While it was not possible to collect neutron data for the 5% LT122 phase in our single-crystal diffraction experiment, we are capable of qualitatively producing the observed x-ray single-crystal diffraction patterns using appropriate space groups that could allow the extra reflections to exist. A combination of group theoretical representation analysis using ISODISTORT and the SINGLECRYSTAL-CRYSTALMAKER software suite was used [46,47]. Analyses of the LT122 and 245 possible superstructures were first performed independently in order to properly assign the extra reflections to the appropriate phase. We examined the effects of moderate strains, displacive (Fe, Cs, and Se), and occupational (Fe and Cs) order parameters. The selenium content was not allowed to change because it consistently refined to full occupancy in addition to the fact that disturbing the selenium content would have drastic effects on the iron local coordination. On the other hand, the special position of the Cs site exhibits no degrees of freedom so it could not contribute to displacive ordering while the Fe and Se sites do allow the ions to move. For the LT122 phase, all $I4/mmm$ subgroups with basis vectors of the type {(1,1,0)(−1,1,0)(0,0,1)} or {(2,0,0)(0,2,0)(0,0,2)} were fully examined. The 245 phase was examined using subgroups of $I4/m$ with basis vectors of the type {(1,0,0)(0,1,0)(0,0,1)} and {(1,0,0)(0,1,0)(0,0,2)}. For both symmetries, basis vector permutations and origin shifts were allowed and examined. Upon comparison of the diverse models with the actual experimental data, we found that none of the displacive Fe and Se modes or the Fe occupational mode could produce all the observed extra reflections. Only Cs occupational ordering allows all the reflections to be accounted for with a qualitative intensity pattern consistent with the experimental data; see Fig. 8.

For the LT122 phase, the transition from the parent $(a \times a \times c)$ $I4/mmm$ symmetry to the $(\sqrt{2}a \times \sqrt{2}a \times c)$ $P4/mmm$ superstructure symmetry is driven by cationic ordering primarily along the X $(\frac{1}{2}\ \frac{1}{2}\ 0)$ k-point direction. A secondary Cs occupational order parameter along the M (111) k point is also needed. The superposition of the X^{1+} and M^{1+} irreps rotates the unit cell of the parent $I4/mmm$ structure by 45° and produces Cs occupational ordering along the

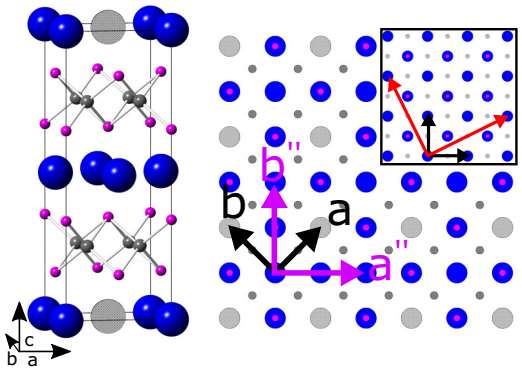

FIG. 8. (Color online) Proposed $\sqrt{2} \times \sqrt{2} \times 1$ Cs vacancy-ordered model with occupied and vacant cesium, iron, and selenium sites indicated by blue, crosshatched gray, solid gray and magenta spheres, respectively. Seen at right is a view along the c axis of the relative size and orientation of the a and b lattice parameters for the HT122 phase (in black), LT122 phase (purple with asterisk), and the standard $\sqrt{5} \times \sqrt{5} \times 1$ supercell of the 245 phase (red vectors in inset).

three-dimensional vector P1(a,a,b) in excellent agreement with the experimental data. Modulations allowed by the occupational A_{1g} modes of the parent Cs $2a$ site resulted in the complete removal of Cs2 in the subgroup $P4/mmm$ superstructure and in increasing the content of Cs1 and Cs3 to full occupancy. It should be noted that the absence of Cs2 corresponds to 25% vacancies of the total Cs stoichiometry in excellent agreement with the refinement results. As shown in Fig. 8, Cs vacancies form exclusively in only one layer between the $FeSe_4$ layers, thus leaving the middle Cs layer full and intact. Our results show that Cs vacancies order three dimensionally as they alternate along the c-axis direction while forming a periodic arrangement in the ab plane with every vacancy surrounded by four occupied Cs sites that can be described as alternating full and vacant Cs sites along the a or b directions of the parent 122 structure; see Fig. 8.

Despite the success of our Cs vacancy-ordered model in qualitatively describing all the diffraction spots of our single crystals, we should not rule out the possibility that other superstructures, possibly with Cs vacancies ordered on different sites (not observed in this work), may form within the same material depending on the growth conditions of the investigated crystals. This is demonstrated by the various reports of intensity rods [18,26] *in lieu of* our observed $(\frac{1}{2}\ \frac{1}{2}\ l)$ and $(\frac{3}{2}\ \frac{3}{2}\ l)$ reflections, for example, and the recent *ab initio* calculations of Ref. [26]. Such intensity rods may then be due to different short-range ordering of the Cs vacancies in addition to low-dimensional Cs correlations within the different domains. The distinctly sharp superlattice reflections confirm the high quality of our crystals and render modeling of the proposed superstructure possible.

Weak reflections were also seen in the 110 plane of the 245 phase at (00l) and (11l) (with l being odd). These are similar to reflections observed with the LT122 superstructure and can be clearly differentiated with large enough l values as shown in Fig. 7(b), for example. While it is puzzling that the well-studied 245 phase may still exhibit further ordering, this possibility cannot be ruled out. As shown in Table I, the $I4/m$ structure of the 245 phase offers 2 Cs sites ($2a$ and $8h$) on which the Cs distribution may or may not be uniform within the crystal or among different crystals depending on the growth conditions and starting compositions of the diverse batches. Nonetheless, we note that the total Cs content per unit formula refines within a few standard deviations to values close to the expected $x(Cs) = 0.8$ stoichiometry. The variation of Cs distribution may then lead to either the appearance or the absence of Cs-ordered structures in the main 245 phase and may explain the fact that such an ordering has never been reported. Additionally, we note that the extremely weak superstructure reflections that belong to Cs ordering in the 245 phase may have been masked by the previously observed LT122 streaky superlattice reflections. The fact that we observe superlattice reflections in our high-quality crystals instead of the streaky reflections or intensity rods allows us to unambiguously assign the different reflections to their corresponding phases.

Indexing the extra peaks with the 245 structure requires changing the lattice type and symmetry from body-centered $I4/m$ to primitive $P4/m$ while keeping the size of the unit cell unchanged. In the $P4/m$ space group symmetry, Cs may occupy four independent Wyckoff sites at $1a$ (0 0 0), $1d$ $(\frac{1}{2}\ \frac{1}{2}\ \frac{1}{2})$, $4j$ (0.4 0.8 0), and $4k$ (0.9 0.3 $\frac{1}{2}$). Again, group theoretical analysis shows similar occupational A_{1g} modes that order the Cs occupancies and vacancies in only one of the two independent layers (the middle layer with $z = \frac{1}{2}$). We find that Cs is fully removed from the $1d$ site and partially and randomly removed from the $4k$ site (25% off the positions allowed by this site) while the remaining two sites are fully occupied. Thus, the overall Cs content is 0.8 in agreement with the refined and expected occupancy of the 245 phase. It should also be noted that adjusting the occupancy of the mostly "vacant" Fe site during modeling did not produce any extra reflections when allowed to vary. Finally, the simulated LT122 superstructure [001] and [110] patterns are shown in Figs. 7(c) and 7(d) overlaid with the patterns of 245 phase twins. The simulated patterns are in excellent agreement with the data.

Due to the fact that microscopic clusters are unavoidably forming during the phase transition and separation to Fe-poor, Cs-rich and Fe-rich, Cs-poor clusters, one could speculate that phases other than the identified LT122 minority phase may also be stabilized either in the form of independent entities or as stacking faults within the host majority phase matrix and/or the minority LT122 phase. While there is no indication of such stacking faults in the majority phase, the often-observed intensity rods could also be interpreted as partially due to their presence (e.g., 11 or 111 atomic thin layers embedded in the 122 structure), thus further weakening the interlayer couplings and possible ordering. In fact, powders obtained by grinding large crystals or by the direct synthesis of $Cs_xFe_{2-y}Se_2$ bulk materials show significant intensities filling the space between the well-resolved 002 peaks of the 245 and the LT122 phases; see Figs. 2(d) and 2(f). We finally speculate that the microscopic minority phases are stabilized while embedded in the host matrix and that grinding the crystals causes these thin domains to break into even smaller pieces below the superconductivity coherence length, therefore destroying their

superconductivity—a conclusion that can further confirm that superconductivity is indeed a property of the microscopic minority phase as long as it remains large enough, continuous, and perhaps percolative. This conclusion is supported by the confirmed growth of nonsuperconducting single crystals in our lab (and by others [33]) in which the minority phase represents no more than an estimated 1%−2% of the total volume. Alternately, we speculate that crystals should remain superconducting when ground if the minority phase fractional amount is beyond the percolation limit of perhaps 40% or more. However, such a sample may be better described as biphasic.

IV. CONCLUSIONS

High-quality $Cs_xFe_{2-y}Se_2$ single crystals were grown using an elaborate multistep synthesis technique. By carefully controlling the starting precursors' and materials' stoichiometry, we demonstrate the existence of a superconducting dome with T_c smoothly evolving as a function of the nominal iron valence. Neutron powder diffraction studies reveal a first-order structural transition at 530 K followed by a decoupled magnetic transition at 490 K in $Cs_{0.9}Fe_2Se_2$. The formation of the vacancy-ordered 245 phase is coincident with the appearance of a minority tetragonal LT122 phase. Using an average tetragonal $I4/mmm$ structure, the atomic positions and lattice parameters of this LT122 phase were extracted and found to diverge significantly from the HT122 phase indicating its discontinuous formation from the HT122 phase. Magnetic peaks of the 245 phase were monitored as a function of temperature by neutron single-crystal diffraction across the superconducting transition and found to show no signs of suppression or correlation with the advent of superconductivity, a competition that is clearly established in other iron-based superconducting arsenides. This result considered along with the observation that upon grinding superconducting crystals become nonsuperconducting is taken as evidence supporting the conclusion that the LT122 phase is the host of superconductivity. In x-ray single-crystal diffraction data, the LT122 phase is seen to have supercell reflections consistent with a $\sqrt{2} \times \sqrt{2} \times 1$ superstructure caused by ordering of the Cs vacancies, a model consistent with the refined Cs occupancy of nearly 75%. The primitive symmetry of the LT122 superstructure indicates the decoupling and formation of independent Cs sites at the alternating layers. Unlike previous reports, discrete diffraction peaks are observed, indicating the three-dimensional ordering of the LT122's Cs vacancies in our single crystals. A second set of weak extra reflections commensurate with the majority 245 phase is also seen and indicates a similar lowering of the structural symmetry from body centered to primitive together with partial ordering of the Cs vacancies in this phase as well. Our results shed light on the complex structure of the majority 245 phase exhibiting both Fe- and Cs-ordered vacancies and on the superstructure of the minority three-dimensional Cs vacancy-ordered LT122 phase.

ACKNOWLEDGMENTS

Work at the Materials Science Division at Argonne National Laboratory was supported by the US Department of Energy, Office of Science, Materials Sciences and Engineering Division. Part of the research conducted at ORNL's High Flux Isotope Reactor and Spallation Neutron Source was sponsored by the Scientific User Facilities Division, Office of Basic Energy Sciences, US Department of Energy. The authors thank A. Huq for providing help during experimental setup and data collection.

[1] D.-X. Mou, L. Zhao, and X.-J. Zhou, Front. Phys. **64**, 410 (2011).
[2] G. R. Stewart, Rev. Mod. Phys. **83**, 1589 (2011).
[3] P. Dai, J. Hu, and E. Dagotto, Nat. Phys. **8**, 2438 (2012).
[4] A. K. Ganguli, J. Prakash, and G. S. Thakur, Chem. Soc. Rev. **42**, 569 (2013).
[5] S. Nandi, M. G. Kim, A. Kreyssig, R. M. Fernandes, D. K. Pratt, A. Thaler, N. Ni, S. L. Bud'ko, P. C. Canfield, J. Schmalian, R. J. McQueeney, and A. I. Goldman, Phys. Rev. Lett. **104**, 057006 (2010).
[6] S. Avci, O. Chmaissem, E. A. Goremychkin, S. Rosenkranz, J.-P. Castellan, D. Y. Chung, I. S. Todorov, J. A. Schlueter, H. Claus, M. G. Kanatzidis, A. Daoud-Aladine, D. Khalyavin, and R. Osborn, Phys. Rev. B **83**, 172503 (2011).
[7] S. Avci, O. Chmaissem, D. Y. Chung, S. Rosenkranz, E. A. Goremychkin, J.-P. Castellan, I. S. Todorov, J. A. Schlueter, H. Claus, A. Daoud-Aladine, D. D. Khalyavin, M. G. Kanatzidis, and R. Osborn, Phys. Rev. B **85**, 184507 (2012).
[8] E. Wiesenmayer, H. Luetkens, G. Pascua, R. Khasanov, A. Amato, H. Potts, B. Banusch, H.-H. Klauss, and D. Johrendt, Phys. Rev. Lett. **107**, 237001 (2011).
[9] M. Yi, Y. Zhang, Z. K. Liu, X. Ding, J. H. Chu, A. F. Kemper, N. Plonka, B. Moritz, M. Hashimoto, S. K. Mo, Z. Hussain, T. P. Devereaux, I. R. Fisher, H. H. Wen, Z. X. Shen, and D. H. Lu, Nat. Commun. **5**, 3711 (2014).
[10] J.-P. Castellan, S. Rosenkranz, E. A. Goremychkin, D. Y. Chung, I. S. Todorov, M. G. Kanatzidis, I. Eremin, J. Knolle, A. V. Chubukov, S. Maiti, M. R. Norman, F. Weber, H. Claus, T. Guidi, R. I. Bewley, and R. Osborn, Phys. Rev. Lett. **107**, 177003 (2011).
[11] J. M. Allred, K. M. Taddei, D. E. Bugaris, S. Avci, D. Y. Chung, H. Claus, C. dela Cruz, M. G. Kanatzidis, S. Rosenkranz, R. Osborn, and O. Chmaissem, Phys. Rev. B **90**, 104513 (2014).
[12] S. Avci, J. M. Allred, O. Chmaissem, D. Y. Chung, S. Rosenkranz, J. A. Schlueter, H. Claus, A. Daoud-Aladine, D. D. Khalyavin, P. Manuel, A. Llobet, M. R. Suchomel, M. G. Kanatzidis, and R. Osborn, Phys. Rev. B **88**, 094510 (2013).
[13] S. Avci, O. Chmaissem, J. M. Allred, S. Rosenkranz, I. Eremin, A. V. Chubukov, D. E. Bugaris, D. Y. Chung, M. G. Kanatzidis, J.-P. Castellan, J. A. Schlueter, H. Claus, D. D. Khalyavin, P. Manuel, A. Daoud-Aladine, and R. Osborn, Nat. Commun. **5**, 3845 (2014).

[14] P. Gao, R. Yu, L. Sun, H. Wang, Z. Wang, Q. Wu, M. Fang, G. Chen, J. Guo, C. Zhang, D. Gu, H. Tian, J. Li, J. Liu, Y. Li, X. Li, S. Jiang, K. Yang, A. Li, Q. Si *et al.*, Phys. Rev. B **89**, 094514 (2014).
[15] T. Qian, X.-P. Wang, W.-C. Jin, P. Zhang, P. Richard, G. Xu, X. Dai, Z. Fang, J.-G. Guo, X.-L. Chen, and H. Ding, Phys. Rev. Lett. **106**, 187001 (2011).
[16] I. A. Nekrasov and M. V. Sadovskii, JETP Lett. **93**, 3 (2011).
[17] A. Ricci, N. Poccia, B. Joseph, G. Arrighetti, L. Barbra, J. Plaisier, G. Campi, Y. Mizuguchi, H. Takeya, Y. Takano, N. L. Saini, and A. Bianconi, Supercond. Sci. Technol. **24**, 082002 (2011).
[18] A. Bosak, V. Svitlyk, A. Krzton-Maziopa, E. Pomjakushina, K. Conder, V. Pomjakushin, A. Popov, D. de Sanctis, and D. Chernyshov, Phys. Rev. B **86**, 174107 (2012).
[19] D. P. Shoemaker, D. Y. Chung, H. Claus, M. C. Francisco, S. Avci, A. Llobet, and M. G. Kanatzidis, Phys. Rev. B **86**, 184511 (2012).
[20] M. V. Roslova, O. I. Lebedev, I. V. Morozov, S. Aswartham, S. Wurmehl, B. Büchner, and A. V. Shevelkov, Inorg. Chem. **52**, 14419 (2013).
[21] V. Y. Pomjakushin, A. Krzton-Maziopa, E. B. Pomjakushina, K. Conder, D. Chernyshov, V. Svitlyk, and A. Bosak, J. Phys.: Condens. Matter **24**, 435701 (2012).
[22] Z. Wang, Y. J. Song, H. L. Shi, Z. W. Wang, Z. Chen, H. F. Tian, G. F. Chen, J. G. Guo, H. X. Yang, and J. Q. Li, Phys. Rev. B **83**, 140505 (2011).
[23] M. Wang, M. Wang, G. N. Li, Q. Huang, C. H. Li, G. T. Tan, C. L. Zhang, H. Cao, W. Tian, Y. Zhao, Y. C. Chen, X. Y. Lu, B. Sheng, H. Q. Luo, S. L. Li, M. H. Fang, J. L. Zarestky, W. Ratcliff, M. D. Lumsden, J. W. Lynn *et al.*, Phys. Rev. B. **84**, 094504 (2011).
[24] W. Li, H. Ding, Z. Li, P. Deng, K. Chang, K. He, S. Ji, L. Wang, X. Ma, J.-P. Hu, X. Chen, and Q.-K. Xue, Phys. Rev. Lett. **109**, 057003 (2012).
[25] W. Bao, Q.-Z. Huang, R.-F. Chen, M. A. Green, D.-M. Wang, J.-B. He, and Y.-M. Qui, Chin. Phys. Lett. **28**, 086104 (2011).
[26] D. G. Porter, E. Cemal, D. J. Voneshen, K. Refson, M. J. Gutmann, A. Bombardi, A. T. Boothroyd, A. Krzton-Maziopa, E. Pomjakushina, K. Conder, and J. P. Goff, Phys. Rev. B **91**, 144114 (2015).
[27] K. G. Vandervoort, G. Griffith, H. Claus, and G. W. Crabtree, Rev. Sci. Instrum. **62**, 2271 (1991).
[28] B. C. Chakomakos, H. Cao, F. Ye, A. D. stoica, M. Popovici, M. Sundaram, W. Zhou, J. S. Hicks, G. W. Lynn, and R. A. Riedel, Appl. Crystallogr. **44**, 655 (2011).
[29] J. Rodriguez-Carvajal, Physica B **192**, 55 (1993).
[30] A. C. Larson and R. B. Von Dreele, General Structure Analysis System (GSAS), Report LAUR 86-748 (Los Alamos National Laboratory, Los Alamos, NM, 2004).
[31] B. H. Toby, J. Appl. Crystallogr. **34**, 210 (2001).
[32] V. Tsurkan, J. Deisenhofer, A. Günther, H.-A. Krug von Nidda, S. Widmann, and A. Loidl, Phys. Rev. B **84**, 144520 (2011).
[33] Y. J. Yan, M. Zhang, A. F. Wang, J. J. Ying, Z. Y. Li, W. Qin, X. G. Luo, J. Q. Li, J. Hu, and X. H. Chen, Sci. Rep. **2**, 212 (2012).
[34] U. Holzwarth and N. Gibson, Nat. Nanotechnol. **6**, 534 (2011).
[35] S. C. Speller, T. B Britton, G. M. Hughes, A. Krzton-Maziopa, E. Pomjakushina, K. Conder, A. T. Boothroyd, and C. R. M. Grovenor, Supercond. Sci. Technol. **25**, 084023 (2012).
[36] S. Landsgesell, D. Abou-Ras, T. Wolf, D. Alber, and K. Prokeš, Phys. Rev. B **86**, 224502 (2012).
[37] N. Lazarevic, M. Abeykoon, P. W. Stephens, H. Lei, E. S. Bozin, C. Petrovic, and Z. V. Popovic, Phys. Rev. B **86**, 054503 (2012).
[38] Y. Texier, J. Deisenhofer, V. Tsurkan, A. Loidl, D. S. Inosov, G. Friemel, and J. Bobroff, Phys. Rev. Lett. **108**, 237002 (2012).
[39] X. G. Luo, W. F. Wang, J. J. Ying, Y. J. Yan, Z. Y. Li, M. Zhang, A. F. Wang, P. Cheng, Z. J. Xiang, G. J. Ye, R. H. Liu, and W. H. Chen, New J. Phys. **13**, 053011 (2011).
[40] F. Ye, S. Chi, W. Bao, X. F. Wang, J. J. Ying, X. H. Chen, H. D. Wang, C. H. Dong, and M. Fang, Phys. Rev. Lett. **107**, 137003 (2011).
[41] Y. J. Long, D. M. Wang, Z. Wang, H. X. Yang, J. B. He, L. X. Zhao, P. P. Wang, M. Q. Xue, J. Q. Li, Z. A. Ren, and G. F. Chen, Phys. Rev. B **90**, 144519 (2014).
[42] V. Y. Pomjakushin, D. V. Sheptyakov, E. V. Pomjakushina, A. Krzton-Maziopa, K. Conder, D. Chernyshov, V. Svitlyk, and Z. Shermadini, Phys. Rev. B **83**, 144410 (2011).
[43] H. Kleinert, Phys. Rev. D **57**, 2264 (1998).
[44] X. Luo, S. Öğüt, and T. Yildirim, Phys. Rev. B **89**, 054519 (2014).
[45] J. Zhao, H. Cao, E. Bourret-Courchesne, D.-H. Lee, and R. J. Birgeneau, Phys. Rev. Lett. **109**, 267003 (2012).
[46] B. J. Campbell, H. T. Stokes, D. E. Tanner, and D. M. Hatch, J. Appl. Crystallogr. **39**, 607 (2006).
[47] CRYSTALMAKER, CrystalMaker Software Ltd, Oxford, UK, www.crystalmaker.com.